Supplementary Information (SI) for Materials Horizons.
This journal is © The Royal Society of Chemistry 2025

Inverse design of isotropic auxetic metamaterials via data-driven strategy

Ertai Cao[†a], Zhicheng Dong[†b], Ben Jia[b], Heyuan Huang[*ac]

[a]*School of Aeronautics, Northwestern Polytechnical University, Xi'an 710072, China.*

E-mail: huangheyuan@nwpu.edu.cn

[b]*School of Civil Aviation, Northwestern Polytechnical University, Xi'an 710072, China*

[c]*Design National Key Laboratory of Strength and Structural Integrity, Xi'an 710072, China*

[†]These authors contribute equally to this manuscript.

1. Size Effect Analysis

To verify whether our constructed model exhibits size effects, we performed a finite element simulation to analyze the influence of unit cell quantity on mechanical performance. As shown in Figure xa, we first constructed array models of various sizes based on Model I (2×2, 4×4, 6×6, 8×8, and 10×10 unit cells), and applied identical boundary conditions (fixed at the bottom, with 20% tensile strain applied at the top). The resulting stress-strain curves under the same loading direction were then compared to assess the variations across different model sizes.

As shown in Figure S1b, the stress-strain curves exhibit a noticeable size effect as the number of unit cells increases. Overall, under the same applied strain, the nominal stress of the simulated model decreases with the increase in the number of unit cells, although the rate of decrease gradually diminishes. As illustrated in Figure xc, the 2×2 unit cell model is significantly influenced by boundary effects, displaying a stress-strain response that differs markedly from those of models with more unit cells, clearly indicating its inaccuracy. To minimize the impact of size effects, it is necessary to select models with a sufficiently large number of unit cells to better approximate the stress-strain response of an infinite planar structure. When the unit cell count reaches 6×6 or greater, the mechanical response tends to stabilize, and the stress deviation at 20% strain remains within 1% even as the unit cell number continues to increase. This indicates that while the 6×6 model exhibits some size effects, it is sufficiently accurate for the purpose of investigating the isotropic stress-strain response in this study. Therefore, the 6×6 unit cell model used in this work is both reliable and representative for exploring the overall deformation and mechanical response of the structure.

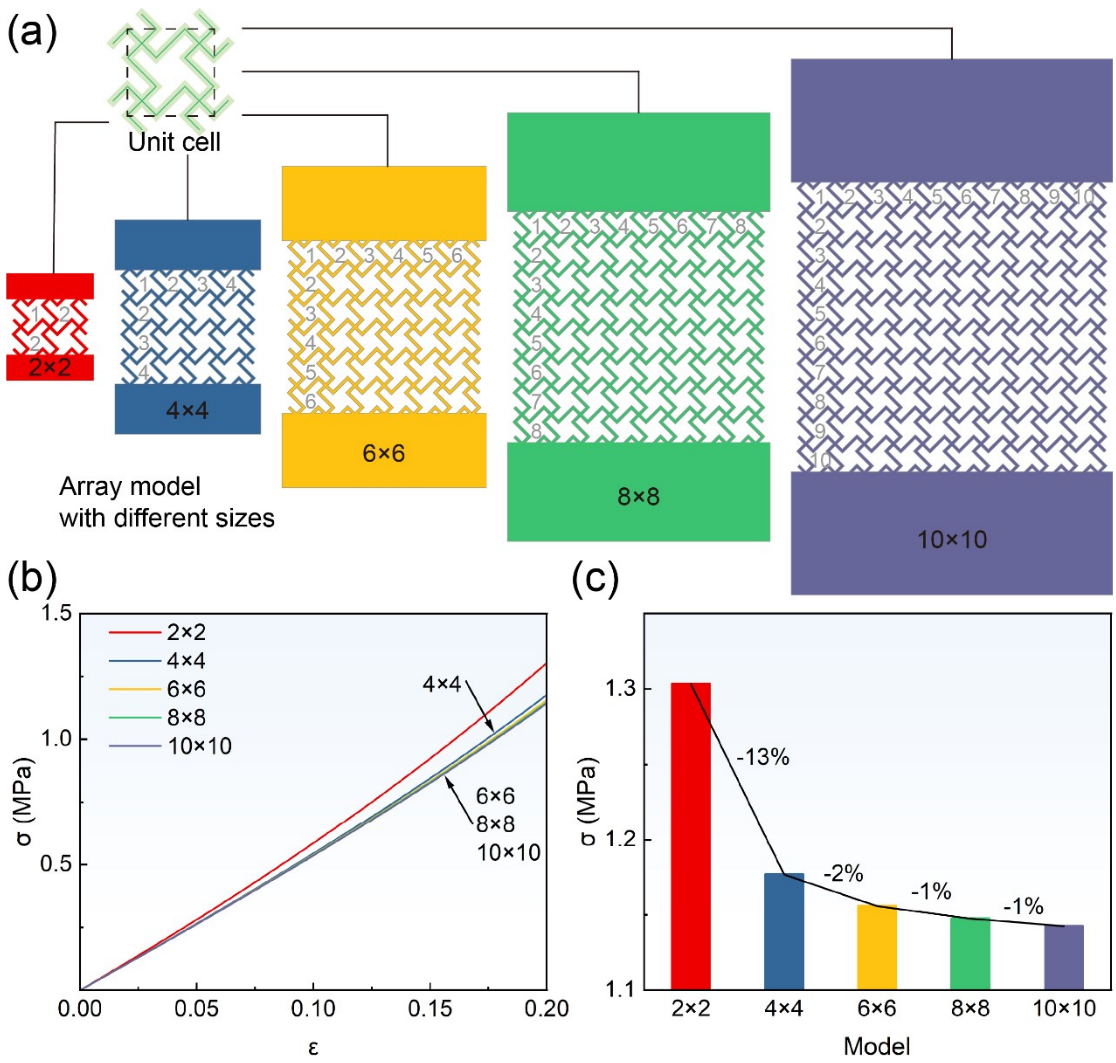

Fig. S1. (a) Array models with different sizes. (b) Stress-strain responses under different sizes. (c) Comparison of response variation with size.

This size effect analysis method refers to the approach used by Chan et al.[1] in their study of chiral three-dimensional isotropic lattices with negative Poisson's ratio.

2. Adaptability of Different Hyperelastic Constitutive Models to Experimental Results

We attempted to fit our experimental results using other hyperelastic constitutive models, including the Yeoh, Neo-Hookean, Arruda-Boyce, Gent, and Ogden models. However, the fitting accuracy of the Mooney-Rivlin model was significantly superior to these alternatives.[2]

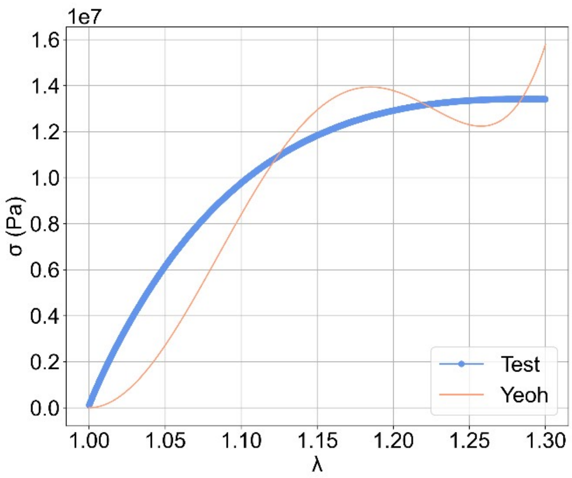

(a) Yeohconstitutive model

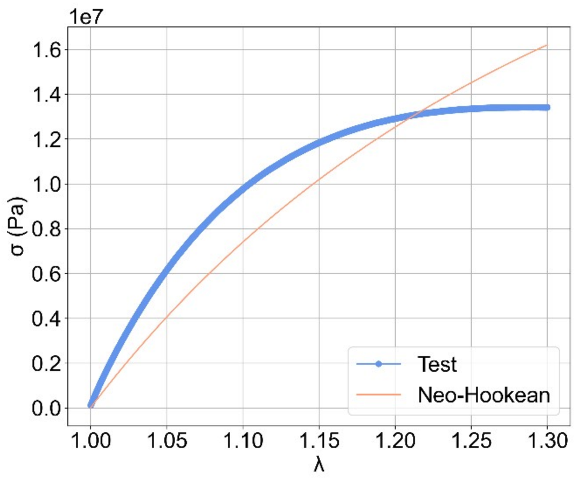

(b) Neo-Hookeanconstitutive model

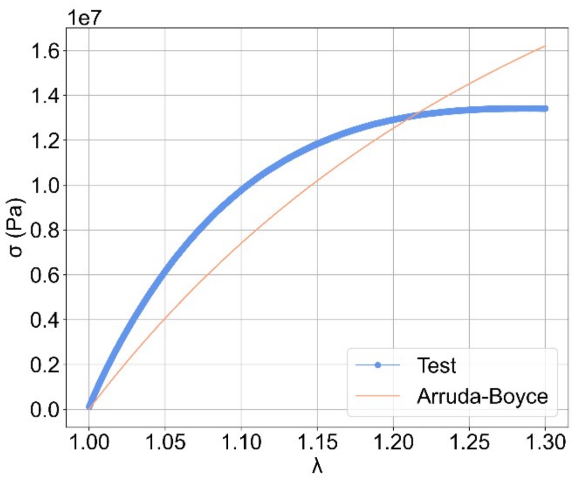

(c) Arruda-Boyceconstitutive model

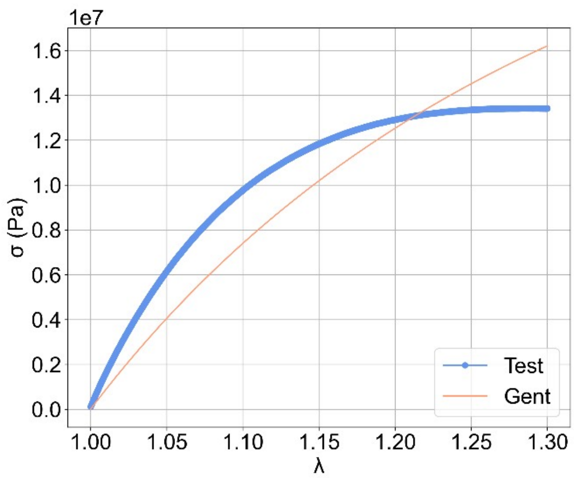

(d) Gentconstitutive model

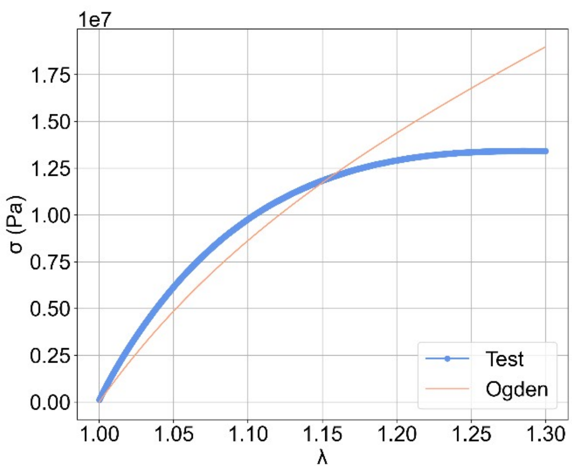

(e) Ogdenconstitutive model

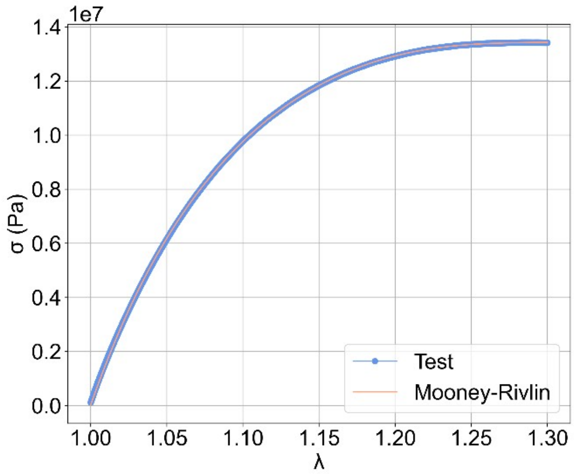

(f) Mooney-Rivlinconstitutive model

Fig. S2. Uniaxial Tensile Test Fitting Results for PCL Specimens Under Different Constitutive Models

3. Comparison between KAN and Other Deep Learning Methods

KAN enhances the model's ability to capture complex functional relationships through hierarchical nonlinear mappings. Its design is inspired by the Kolmogorov-Arnold theorem, which states that any multivariate continuous function can be represented using a finite number of nonlinear basis functions. Therefore, KAN possesses strong functional approximation capabilities. Compared to traditional neural networks, KAN can represent complex mappings with fewer parameters and shallower architectures, thereby reducing computational redundancy. Through nonlinear transformations, KAN is able to more compactly extract deep features from the data. Due to its architectural properties, KAN also demonstrates improved training stability compared to conventional neural networks. This is particularly evident in large-scale datasets, where KAN shows a reduced tendency to overfit.

The following table summarizes the comparison between KAN and other methods:

Table S1. Comparison between KAN and Other Deep Learning Methods

Feature	KAN[3]	MLP[4]	CNN[5]	GAN[6]
Expressive Power	Strong, suitable for complex nonlinear mappings	Moderate, limited to linear combinations	Strong, suitable for processing image data	Strong, suitable for generative tasks
Training Stability	High, avoids overfitting issues	Prone to overfitting	High, especially for image tasks	Unstable, prone to mode collapse
Suitable Tasks	High-dimensional, complex data, especially nonlinear tasks	Basic classification and regression tasks	Image, video, and spatial data	Generative models, especially adversarial training tasks
Interpretability	High, symbolic representation and structured explanation through pruning	High, simple model structure	High, convolutional and pooling layers are easy to explain	Low, complex interactions between generator and discriminator

4. Comparison Between Conventional Design Methods and Inverse Design Strategies

Our method incorporates inverse design combined with a data-driven approach, allowing the introduction of more degrees of freedom during optimization. This strategy considers geometric symmetry and isotropic stress-strain responses of the material, thereby enabling the design of materials with greater accuracy and efficiency. Through this approach, we can not only identify optimal solutions within the predefined design space but also validate and refine the design process itself, significantly enhancing design feasibility and efficiency.

Based on the above discussion, we have provided a comparative analysis of conventional and inverse design methods under optimization conditions, as summarized in the following comparative table:

Table S2. Comparison of conventional design method and inverse design method

Comparison Aspects	Conventional Design Method	Inverse Design Method
Design Approach	Based on experience and intuition; performance is optimized by adjusting structural parameters (e.g., edge length, curvature)	Starts from target performance and uses algorithms to inversely derive the required microstructural features for precise design.
Optimization Target	Macroscopic structural parameters, focusing on the overall shape.	Microstructural features, emphasizing precise control at the detailed level.
Design Process	Trial and error, often requiring multiple iterations to achieve the desired outcome.	Numerical optimization and computational simulations enable rapid convergence to the optimal solution.
Interpretability	Easy to implement but often relies on biomimicry or engineering expertise.	The design outcome directly corresponds to performance metrics, offering clear interpretability.
Computational Cost	Requires substantial computational resources due to repeated simulations and tests.	Optimization algorithms reduce computational load and enhance design efficiency.
Applicability	Suitable for improving existing design frameworks and depends on designer experience.	Suitable for applications requiring precise performance control and systematic design space exploration.

5. Comparison of testing and simulating process among Model III

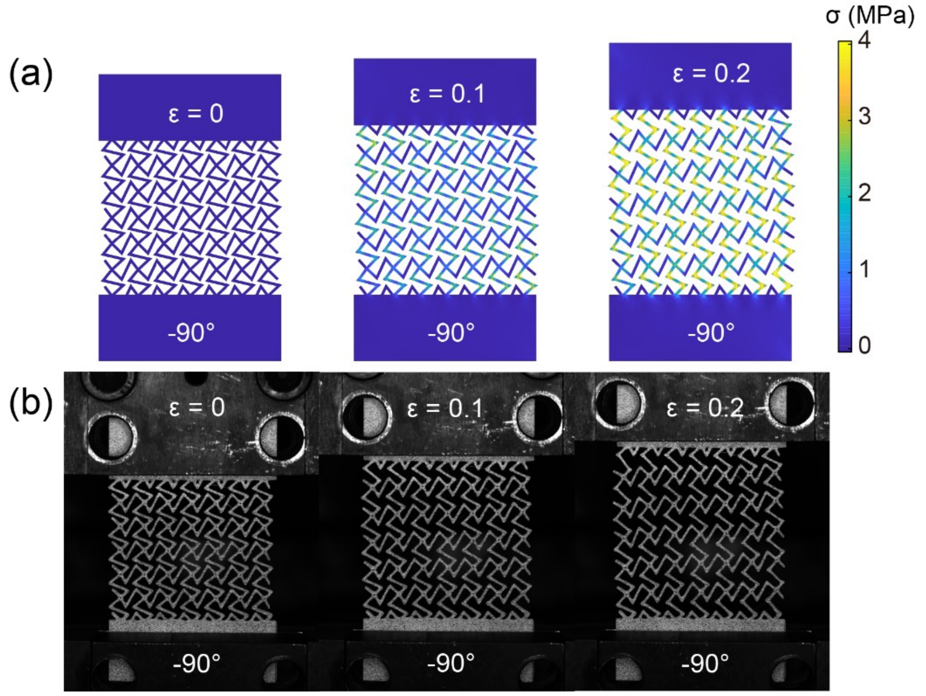

Fig. S3. Comparison of (a) testing and (b) simulating process among Model III under -90°.

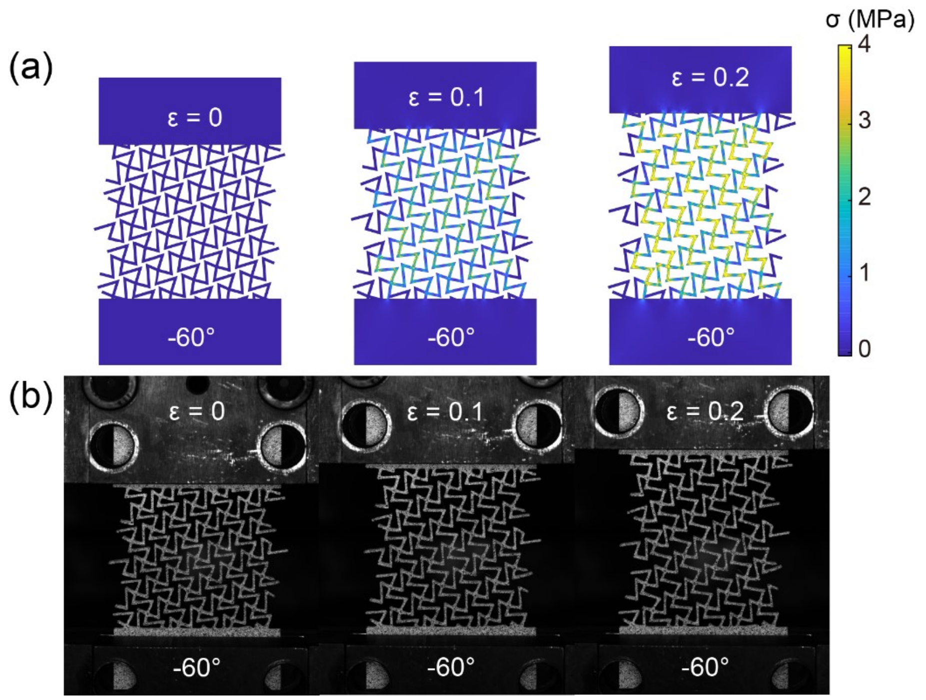

Fig. S4. Comparison of (a) testing and (b) simulating process among Model III under -60°.

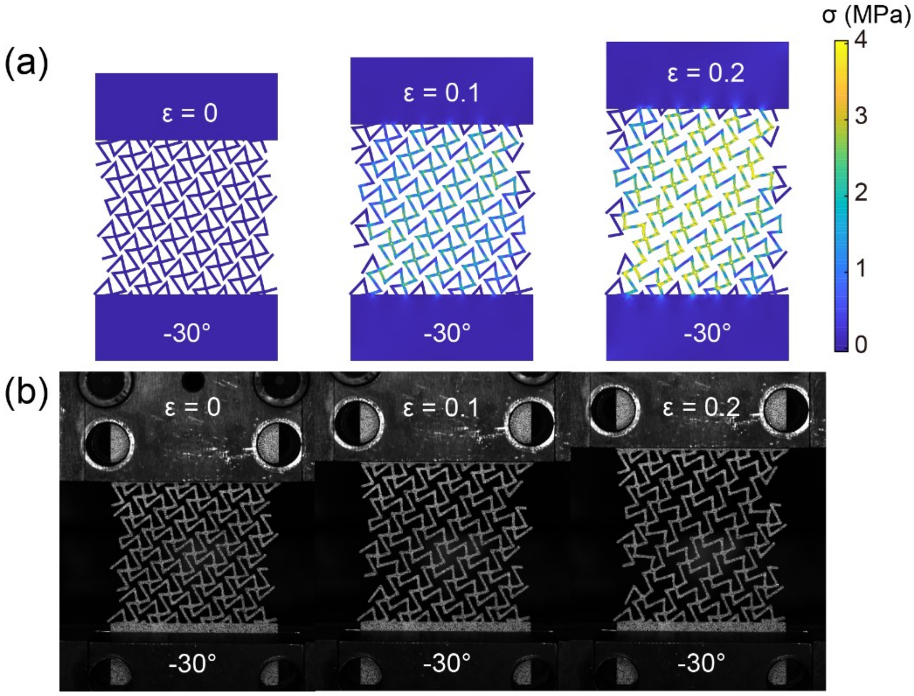

Fig. S5. Comparison of (a) testing and (b) simulating process among Model III under -30°.

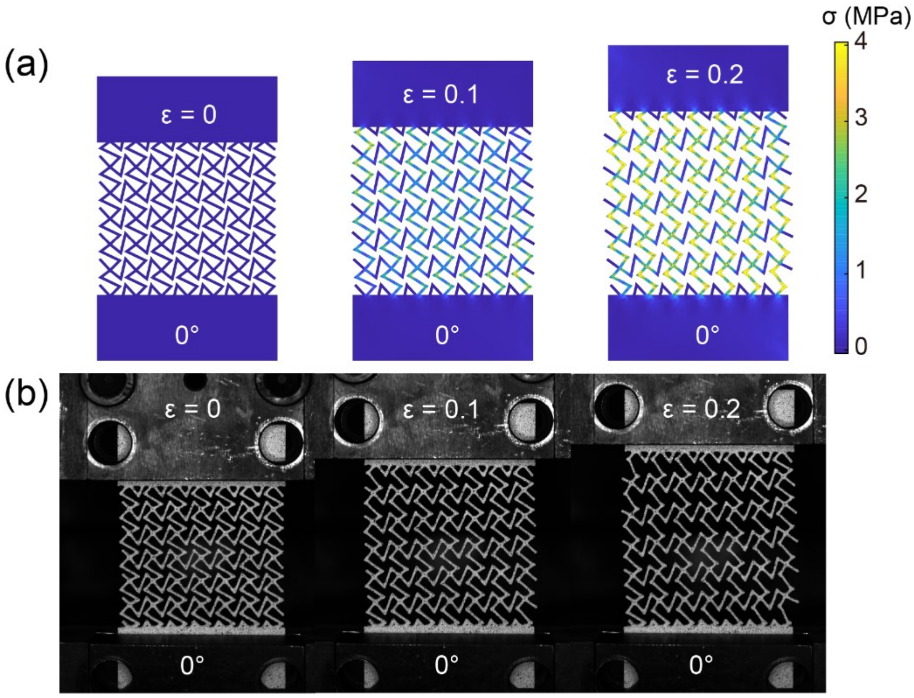

Fig. S6. Comparison of (a) testing and (b) simulating process among Model III under 0°.

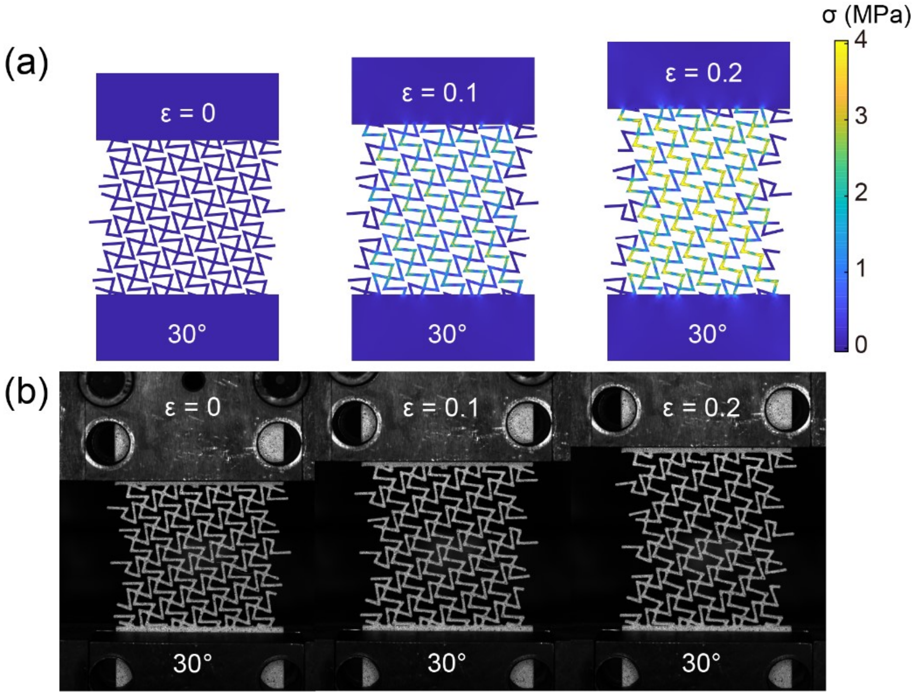

Fig. S7. Comparison of (a) testing and (b) simulating process among Model III under 30°.

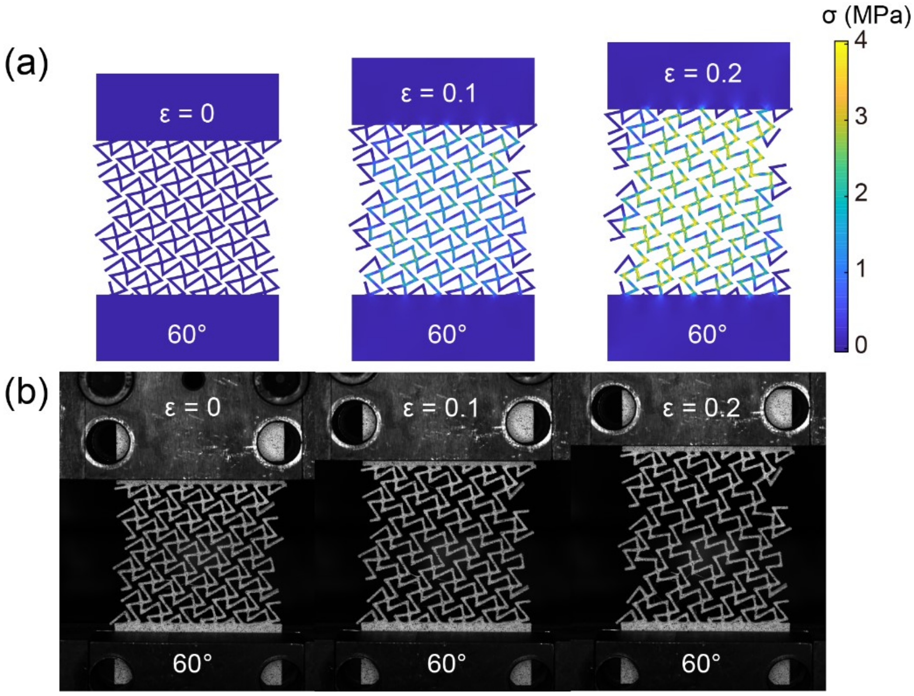

Fig. S8. Comparison of (a) testing and (b) simulating process among Model III under 60°.

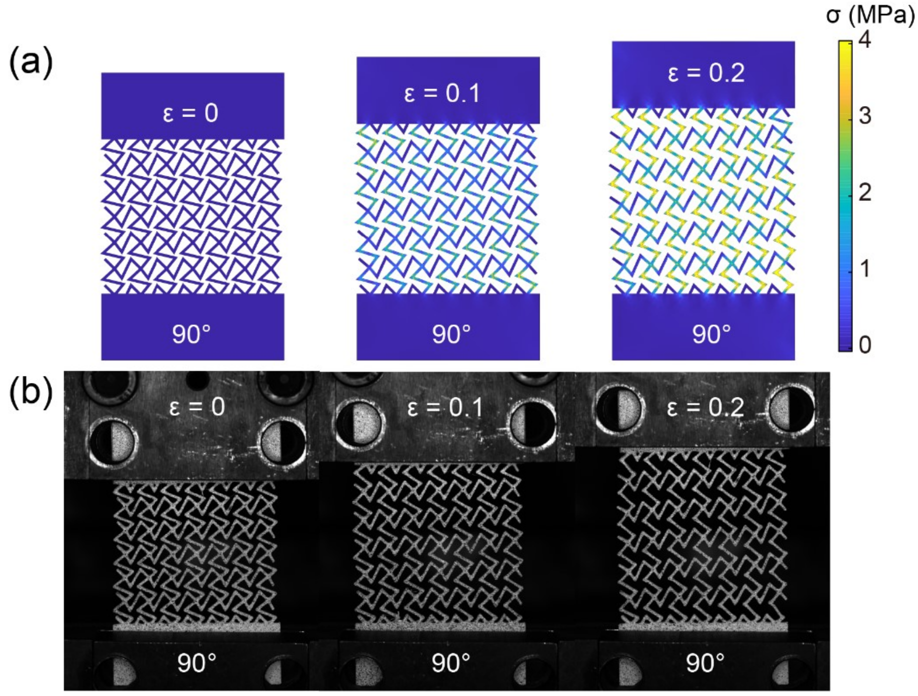

Fig. S9. Comparison of (a) testing and (b) simulating process among Model III under 90°.

6. Comparison of Design Parameters and Stress-Strain Responses of the Three Models

In the final design, Model III exhibits greater consistency in isotropic stress responses, and stress concentration issues are significantly mitigated. As a result, Model III demonstrates superior mechanical performance, particularly in terms of response uniformity under multi-directional loading. Compared with Models I and II, Model III outperforms both in experimental and simulation evaluations.

The design parameters for the three models are listed in Table S3.

Table S3. Design parameters of the three models

Model	e_{1x} (mm)	e_{1y} (mm)	e_{2x} (mm)	e_{2y} (mm)	e_{3x} (mm)	e_{3y} (mm)	e_{4x} (mm)	e_{4y} (mm)
I	0	0	0	0	0	0	0	0
II	0.2	-1	1	-1	-0.25	-1	1	-0.25
III	1.3048	-0.6511	-1.2426	1.5	-0.8941	-0.1863	0.9578	1.0032

Table S3 presents the stress-strain responses of the three models under different loading directions, as well as the mean square error (MSE) between each directional response and the average response. As shown, Model III exhibits significantly lower MSE values across all directions compared to Models I and II. These results are also visualized in the main text through heatmaps in Figures 13b–d.

Table S4. Stress-strain responses of the three models and corresponding MSEs with the directional average

Model	Direction (°)	$\sigma_{0.1}$ (MPa)	$\sigma_{0.2}$ (MPa)	MSE
Model I	-90	0.5390	1.1560	2.6317%
	-60	0.2507	0.5130	3.8124%
	-30	0.3837	0.7547	0.2361%
	0	0.5389	1.1557	2.6266%
	30	0.2506	0.5129	3.8146%
	60	0.3836	0.7546	0.2368%
	90	0.5389	1.1558	2.6278%
	Average	0.4122	0.8575	**2.2837%**
Model II	-90	0.4857	1.0331	3.6219%
	-60	0.2320	0.4703	1.5066%
	-30	0.2854	0.5459	0.4966%
	0	0.3357	0.6766	0.0006%
	30	0.1864	0.3641	3.2639%
	60	0.3360	0.6660	0.0047%
	90	0.4859	1.0334	3.6314%
	Average	0.3353	0.6842	**1.7894%**
Model III	-90	0.2456	0.4826	0.0023%
	-60	0.2379	0.4491	0.0115%
	-30	0.2519	0.4754	0.0035%
	0	0.2765	0.5519	0.1838%
	30	0.2327	0.4424	0.0238%
	60	0.2226	0.4165	0.0843%
	90	0.2441	0.4795	0.0011%
	Average	0.2445	0.4711	**0.0443%**

7. Comparison of Stress Distributions of Model III under Varying Strains

As shown in Figure S10, our optimized model exhibits a near-circular response similar to that of sixfold or threefold symmetric structures at small strain. This indicates that our optimization has effectively enhanced isotropy and suppressed stress concentration within that range. However, as the strain increases and approaches the material's performance limits, nonlinear effects may manifest in all structures-regardless of their symmetry-explaining why, despite high optimization precision, our model still shows slight deviations from a perfect circle.

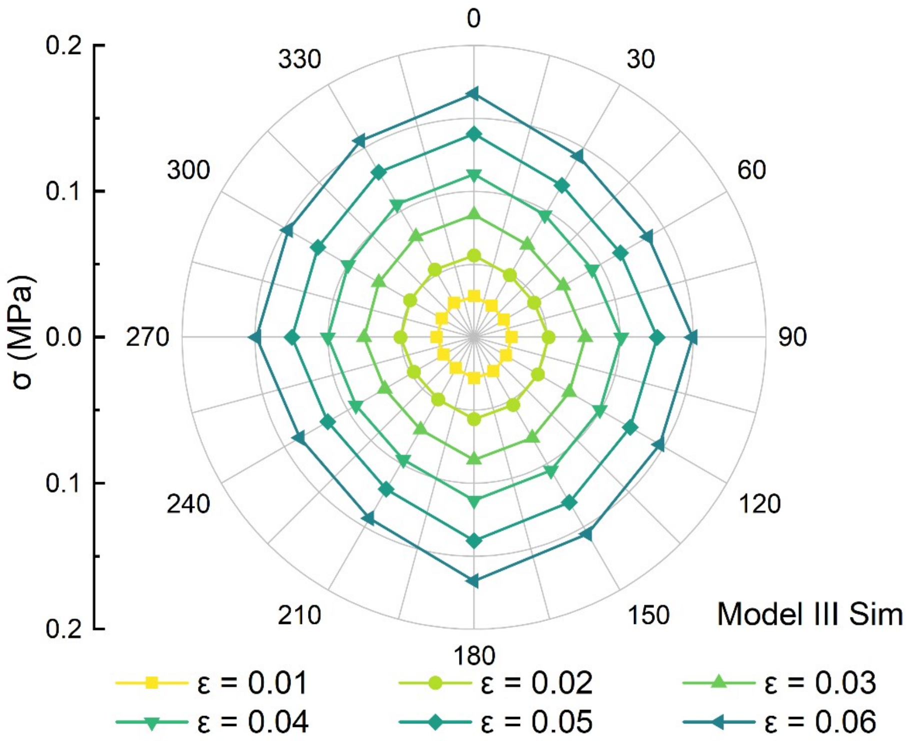

Fig. S10. Stress Distributions of Model III under Different Strain Levels

8. Symmetry Analysis

For our classical missing-rib auxetic structure, Model I, the initial geometric configuration exhibits symmetry in specific directions (e.g., 0° and 90°), but it is not fully isotropic. Its stiffness matrix corresponds to the orthotropic symmetry group (D_2),[7] which includes three independent elastic constants. A representative form of the stiffness matrix is given as follows:

$$C^{\text{hom}} = \begin{bmatrix} C_{11} & C_{12} & 0 \\ C_{21} & C_{22} & 0 \\ 0 & 0 & C_{33} \end{bmatrix}$$

Where $C_{11} \neq C_{22}$ and $C_{33} \neq \dfrac{C_{11} - C_{12}}{2}$. This form corresponds to the characteristics of the orthotropic symmetry group (D_2), which features three independent elastic constants.

In contrast, our target isotropic structure, Model III, was optimized using KAN combined with a genetic algorithm, resulting in stress distributions that are uniform in all directions (see Figures 12c and 13a). Its stiffness matrix is expected to conform to the isotropic symmetry group (O(2)), which requires only two independent parameters:

$$C^{\mathrm{hom}} = \begin{bmatrix} C_{11} & C_{12} & 0 \\ C_{12} & C_{22} & 0 \\ 0 & 0 & \dfrac{C_{11} - C_{12}}{2} \end{bmatrix}$$

In the experiments, the stress distribution of Model III was nearly circular (Figure 12c), and the average MSE was as low as 0.05%, confirming that its stiffness matrix satisfies isotropic symmetry.

9. Simulation and Experimental Evaluation of Poisson's Ratio

Poisson's ratio (ν) is typically defined as the ratio of axial strain in one direction to the transverse strain perpendicular to that direction. For planar materials, it can be considered as the ratio between longitudinal and lateral strain.

As shown in Figure 14a, in our study, Poisson's ratio was calculated based on the displacement of specific nodes measured via digital image correlation (DIC). Four approximately square-shaped intersection nodes on the specimen were marked as points 1, 2, 3, and 4 to facilitate displacement tracking. The stereoscopic high-speed camera was configured with appropriate frame rate, exposure time, height, and focal length, and images were captured every 0.1 seconds until the structure was damaged to a point where tracking was no longer feasible. By tracking the displacement of the selected DIC points, the lateral strain was obtained from the horizontal displacement between points 1 and 3, while the longitudinal strain was calculated from the vertical displacement between points 1 and 2. The Poisson's ratio was then computed using the following formula:

$$\nu = \frac{\varepsilon_x}{\varepsilon_y}$$

In the above equation, ν represents the Poisson's ratio of the structure, ε_x is the transverse strain, and ε_y is the longitudinal strain.

In traditional studies of missing-rib auxetic structures, particularly under standard loading directions (e.g., -90°, 0°, and 90°), this point-based measurement method allows for selecting three points within a square or rectangular region, which can directly characterize the Poisson's ratio under small strain conditions. However, for non-horizontal or non-vertical loading directions explored in this study (e.g., -60°), the calculated Poisson's ratio serves only as an approximate representation.

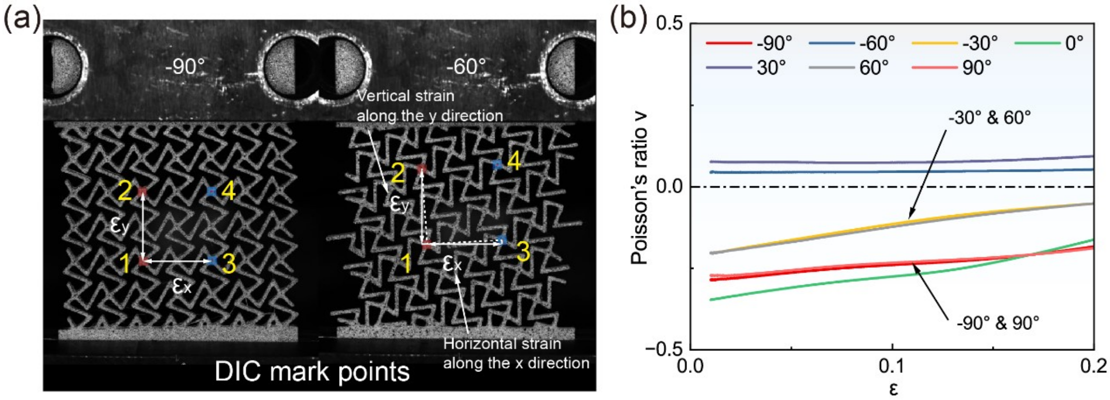

Fig. 14. Measurement of the Poisson's ratio of Model I, Model II, and Model III: (a) Calculation of Poisson's ratio changes using the DIC-based point selection and displacement measurement method; (b) Poisson's ratio variation under different directions of Model III as the strain increases from 0 to 0.2.

For the simulations, we used COMSOL Multiphysics to build the finite element model and apply tensile loads in various directions. The resulting strain distributions were used to calculate the Poisson's ratio.

Specifically, to compute Poisson's ratio from the finite element model, multiple probe points were defined at specific locations within the model. As shown in Figure x, three sets of probes were placed to correspond with the DIC marker points 1, 2, and 3 in Figure 14a. Since it is not possible to directly assign a probe to the central intersection node in COMSOL Multiphysics, each probe set consists of four points surrounding the intersection. The average of these four points was taken to represent the central node.

For example, in probe location 1, four variables were defined for the surrounding points: x10, x1, y10, and y1, with expressions root.X, root.X + u, root.Y, and root.Y + v, respectively (all in mm). Here, root.X and root.Y represent the initial coordinates of the central node, while u and v denote displacements in the x and y directions. Therefore, root.X + u and root.Y + v indicate the deformed coordinates of the intersection point under a given steady-state displacement.

Similarly, for probe location 2, the variables x20, x2, y20, and y2 were defined; and for probe location 3, x30, x3, y30, and y3 were defined. Finally, the variables strain_x, strain_y, and nu were defined as shown in Table 6, corresponding to the transverse strain ε_x, longitudinal strain ε_y, and Poisson's ratio ν, respectively.

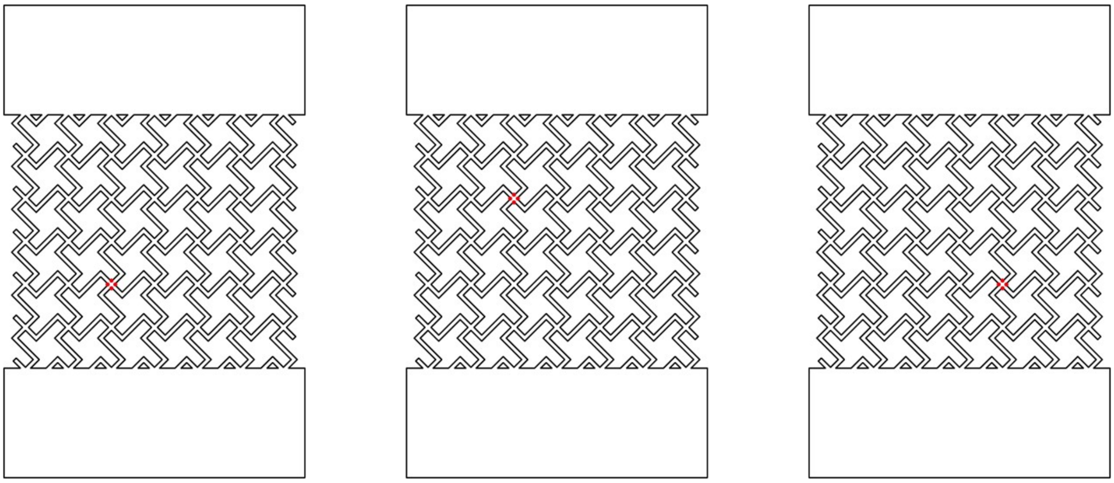

(a) Probe Location 1 (b) Probe Location 2 (c) Probe Location 3

Fig. S11. Schematic of probe locations

Table S5. Operators for Poisson's ratio calculation expressions

Name	Expression
strain_x	((x3-x1)-(x30-x10))/(x30-x10)
strain_y	((y1-y2)-(y10-y20))/(y10-y20)
nu	-strain_x/strain_y

10. Isotropic Analysis of Shear Stress-Strain Responses of Model III

We constructed a finite element model of a 6×6 unit array based on optimized geometric parameters and simulated its nonlinear stress-strain response under shear across various loading directions. The boundary conditions involved fixing the model's lower end and applying shear displacement (up to 20% strain) at the upper end, covering seven loading directions from -90° to 90°.

The shear stress-strain curves indicate that Model III's responses across multiple directions significantly deviate from the average (see Fig. S12), illustrating that achieving isotropy in tensile responses does not necessarily translate to isotropy in shear responses.

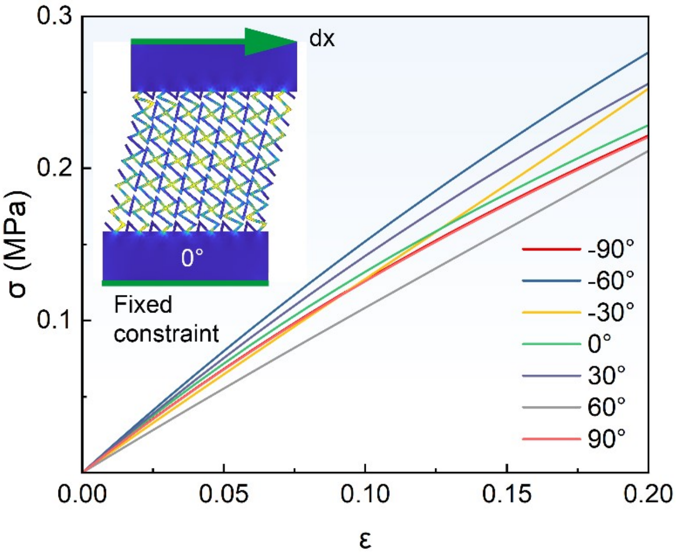

Fig. S12. Shear stress-strain responses of model III under multiple loading directions.

Reference

1 C. S. Ha, M. E. Plesha and R. S. Lakes, *Phys. Status Solidi B Basic Solid State Phys.*, 2016, **253**, 1243–1251.

2 B. Kim, S. B. Lee, J. Lee, S. Cho, H. Park, S. Yeom and S. H. Park, *Int. J. Precis. Eng. Manuf.*, 2012, **13**, 759–764.

3 Z. Liu, Y. Wang, S. Vaidya, F. Ruehle, J. Halverson, M. Soljačić, T. Y. Hou and M. Tegmark, *arXiv:2404.19756*, DOI:10.48550/arXiv.2404.19756.

4 M.-C. Popescu, V. E. Balas, L. Perescu-Popescu and N. Mastorakis, *WSEAS Trans. Circuits Syst.*, 2009, **8**, 579–588.

5 R. Girshick, in *2015 IEEE International Conference on Computer Vision (ICCV)*, IEEE Computer Society, Santiago, Chile, 2015, pp. 1440–1448.

6 I. Goodfellow, J. Pouget-Abadie, M. Mirza, B. Xu, D. Warde-Farley, S. Ozair, A. Courville and Y. Bengio, *Commun. ACM*, 2020, **63**, 139–144.

7 X.-N. Do, V. Calisti and J.-F. Ganghoffer, *Control Cybern.*